

# Tuning the Inter-Nanoplatelet Distance and Coupling Strength by Thermally Induced Ligand Decomposition

Shuai Chen, Samir H. Al-Hilfi, Guangbo Chen, Heng Zhang, Wenhao Zheng, Lucia Di Virgilio, Jaco J Geuchies, Junren Wang, Xinliang Feng, Andreas Riedinger, Mischa Bonn, and Hai I. Wang\*

CdSe nanoplatelets (NPLs) are promising 2D semiconductors for optoelectronic applications, in which efficient charge transport properties are desirable. It is reported that thermal annealing constitutes an effective strategy to control the optical absorption and electrical properties of CdSe NPLs by tuning the inter-NPL distance. Combining optical absorption, transmission electron microscopy, and thermogravimetric analysis, it is revealed that the thermal decomposition of ligands (e.g., cadmium myristate) governs the inter-NPL distance and thus the inter-NPL electronic coupling strength. Employing ultrafast terahertz spectroscopy, it is shown that this enhanced electronic coupling increases both the free carrier generation efficiency and the short-range mobility in NPL solids. The results show a straightforward method of controlling the interfacial electronic coupling strength for developing functional optoelectronic devices through thermal treatments.

## 1. Introduction

Colloidal nanocrystals (NCs) are solution-processable building blocks for cost-efficient electrical and optoelectronic devices,<sup>[1–3]</sup> including field effect transistors, light-emitting diodes, photovoltaics, and photodetectors.<sup>[4–7]</sup> Among different NCs (0D quantum dots (QDs),<sup>[8]</sup> 1D nanorods, etc.),<sup>[9]</sup> CdSe nanoplatelets (NPLs) are promising 2D semiconductors with lateral extension up to over 100 nm<sup>2</sup> and an atomically precise thickness.<sup>[10–12]</sup> The confinement in the thickness direction, which is tunable by controlling the NPLs' layer numbers, has been shown to dominate the electronic and optical properties of CdSe NPLs.<sup>[13,14]</sup> Due to 2D quantum confinement and reduced dielectric screening, photogenerated electrons and holes in NPLs are subject to enhanced Coulomb interactions. This leads to the formation

of strongly bound electron–hole pairs, so-called excitons in NPLs. So far, an extremely high exciton binding energy, that is, the ionization energy needed to dissociate excitons into free carriers, on the order of over 100s of meV has been reported in CdSe NPLs (e.g.,  $\approx 170$  meV for four monolayer (ML) NPLs).<sup>[15,16]</sup> The strong exciton effect results in excellent optical properties including giant oscillator strength,<sup>[17,18]</sup> and strong fluorescence quantum yields<sup>[19]</sup> (up to unity, which is highly desirable for light emission applications).

In conjunction with the thickness-tunable excellent optical properties, the 2D geometry makes NPLs ideal materials to potentially conduct charge carriers for light-to-electrical energy conversion applications, including solar cells and light detectors. In this regard, understanding the exciton dissociation and free carrier generation mechanism in NPLs solids is fundamentally important for high-performance electronic and optoelectronic devices.


The key to achieving efficient free carrier generation and enhanced charge transport properties (e.g., high carrier mobility) lies in “connecting” the NCs to allow sufficiently strong inter-NC electronic coupling. The coupling strength between NCs has been well-known and shown to increase exponentially with decreasing NC-NC distance.<sup>[20–26]</sup> In the QD community, so far, two methods have been demonstrated to effectively modulate the

S. Chen, S. H. Al-Hilfi, H. Zhang, W. Zheng, L. D. Virgilio, J. J. Geuchies, J. Wang, A. Riedinger, M. Bonn, H. I. Wang  
Max Planck Institute for Polymer Research  
Ackermannweg 10, 55128 Mainz, Germany  
E-mail: wanghai@mpip-mainz.mpg.de

G. Chen, X. Feng  
Center for Advancing Electronics Dresden (cfaed) and Faculty of Chemistry and Food Chemistry  
Technische Universität Dresden  
Mommsenstr. 4, 01062 Dresden, Germany

X. Feng  
Max Planck Institute of Microstructure Physics  
D-06120 Halle (Saale), Germany

H. I. Wang  
Nanophotonics  
Debye Institute for Nanomaterials Science  
Utrecht University  
Princetonplein 1, Utrecht 3584 CC, The Netherlands

 The ORCID identification number(s) for the author(s) of this article can be found under <https://doi.org/10.1002/smll.202308951>

© 2023 The Authors. Small published by Wiley-VCH GmbH. This is an open access article under the terms of the Creative Commons Attribution License, which permits use, distribution and reproduction in any medium, provided the original work is properly cited.

DOI: 10.1002/smll.202308951

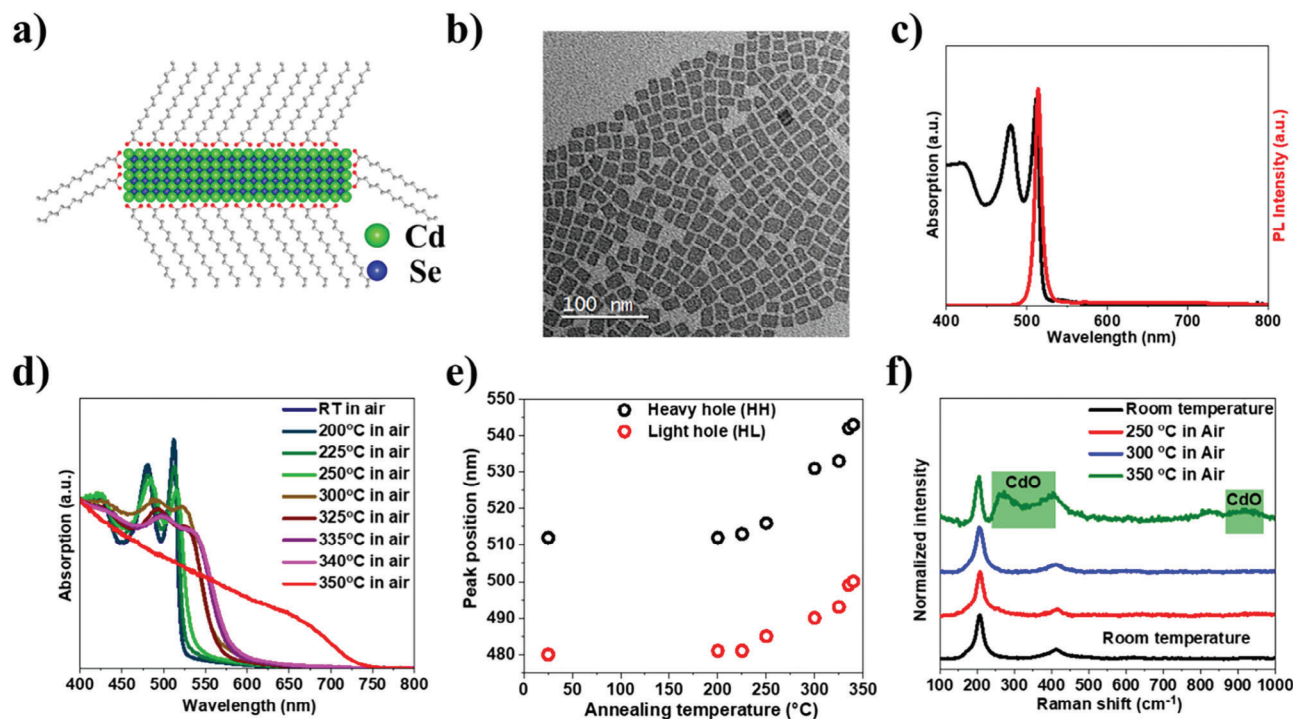


**Figure 1.** Characterizations of four ML CdSe NPLs. a) Atomic structure illustration of four ML CdSe NPLs, which contain five ML of Cd atoms and four ML Se in the structure. The chelating carboxylate ligand is bound to the surface Cd atom to make the system charge neutral. b) The TEM image of face-down four ML CdSe NPLs. c) Absorption (black) and PL emission (red) spectra of four ML CdSe NPLs. d) Temperature-dependent absorption spectra and e) the inferred absorption peaks of four ML CdSe NPLs in air. f) Raman spectra of the four ML CdSe NPLs film with native ligands (black), annealing at 250 °C (red), 300 °C (blue), and 350 °C (olive) in the air.

distance between NCs and thus their coupling strength: ligand exchange and thermal annealing. First, replacing the lengthy native ligands (e.g., cadmium myristate) with shorter ones (including both organic and inorganic) has been widely investigated.<sup>[21–23,27]</sup> For instance, Talapin et al. employed short inorganic ligands ( $S^{2-}$ ,  $SnS_6^{4-}$ ,  $Te^{2-}$ ,  $Se^{2-}$ , or  $HSe^-$ ) to cap QDs and achieved band-like transport in their solids with high electron mobility and photoconductivity.<sup>[28,29]</sup> Second, the key idea behind the thermal annealing strategy lies in removing surface ligands to gradually “fuse” QDs, which leads to an enhanced photoresponse. For instance, octylamine-capped PbS NCs annealed at 220 °C were reported to show a 200-fold increase in the short circuit current.<sup>[30]</sup> CsPbX<sub>3</sub> NCs were shown to possess significantly increased photocurrent after annealing.<sup>[31,32]</sup> CdSe NCs exhibited excellent electrochemical photocurrent, even after a mild heating treatment at 200 °C.<sup>[33]</sup>

In comparison to the QD field, there are fewer experimental efforts toward fabricating strongly coupled NPL solids and understanding their charge transport properties. In this direction, some preliminary work has been done by employing ligand exchange in 2D NPLs. For instance, Nadja et al. synthesized polymer-encapsulated NPL stacks and then manipulated the NPL–NPL distance. Reducing the inter-NPL distance, as expected, increases the photocurrent in devices.<sup>[26]</sup> While effort is still needed to understand the ligand exchange in 2D NPLs, even less research effort has been made to understand one of the most intuitive ways for linking NPLs: thermal annealing. This method

should allow modulating inter-NC distance, and thereby optical properties and charge transport, in a very straightforward manner.

In this work, we combine optical absorption, transmission electron microscopy (TEM), and thermogravimetric analysis with mass spectroscopy (TGA-MS), and provide experimental evidence that the thermal stability of the surface ligands (e.g., their thermal decomposition) governs the inter-NPL distance and thus electronic coupling strength. Employing ultrafast terahertz (THz) spectroscopy, we show that the enhanced electronic coupling increases the free carrier generation efficiency as well as the short-range mobility in NPL solids. Our study provides a new insight for employing thermal treatments as an intuitive and effective method to tune the optical and electrical properties of NPL solids.

## 2. Results and Discussion

### 2.1. Synthesis and Characterization

In the study, we used four ML CdSe NPLs with zinc blende structure, which were prepared following the method reported by Ithurria.<sup>[10]</sup> As illustrated in Figure 1a, the NPLs consisted of 4.5 CdSe monolayers. The TEM images revealed rectangular-shaped 4 ML CdSe NPLs with lateral sizes of  $12.0 \pm 3.4$  by  $15.7 \pm 2.6$  nm (Figure 1b). The absorption spectra possess two pronounced excitonic peaks at 512 and 480 nm as shown in Figure 1c, which can be assigned to the heavy hole (HH) and the light hole

(LH) transitions respectively.<sup>[13,34]</sup> The photoluminescence (PL) emission peak at 513 nm has a full width at half-maximum (FWHM) below 9 nm (equivalently, 32.5 meV) (Figure 1c). Both absorption and PL data are consistent with results previously reported for 4 ML CdSe NPLs.<sup>[12]</sup>

To understand the effect of different annealing treatments on the ligand thermal stability and tuning the inter-NPL distance (and thus the electronic coupling strength), we combine optical absorption, TEM, TGA, and THz spectroscopy to characterize 4 ML CdSe NPLs in thin-films using different annealing temperatures (T). The samples are prepared by drop-casting 20  $\mu\text{L}$  solutions of as-synthesized 4 ML CdSe NPLs ( $1.07 \times 10^{-6}$  M, estimated from the absorption spectrum) on fused silica substrates (1 cm  $\times$  1 cm). The as-prepared NPLs film was annealed in a tube furnace heated to a target T between 200–350 °C for 30 min in the air (for more details, see the supporting information). Samples are then cooled down to room temperature in 120 min for further characterization.

## 2.2. UV-Vis Analysis

As shown in Figure 1d, increasing the annealing T leads to a gradual change in the optical absorption including a significant redshift of the lowest exciton (i.e., the HH transition) transition, when going beyond  $\approx 250$  °C. Annealing treatments are expected to reduce the distance between the NPLs by presumably removing the capping ligands (see the discussion on the detailed mechanism later).<sup>[33,35–38]</sup> This results in enhanced inter-NPL coupling strength and thus loosened quantum and dielectric confinement in NPLs, which explains the absorption changes. Above 340 °C, a gentle increase of annealing T (e.g., from 340 to 350 °C) triggers a sudden transition from a sharp excitonic-like transition to a broader absorption feature with an absorption onset shift from 543 to  $\approx 700$  nm. The inferred bandgap energy (see the Tauc plot in Figure S1, Supporting Information) is 1.70 eV for the sample which was annealed at 350 °C and is close to the bandgap of the bulk CdSe (1.74 eV or  $\approx 710$  nm).<sup>[39,40]</sup> This result indicates that NPLs are fused into bulk-like aggregates (see TEM images below and in Figure S2, Supporting Information) above an annealing T of 340 °C.

## 2.3. Raman Spectroscopy Analysis

To further shed light on the thermal annealing procedure, we performed Raman spectroscopy on NPLs film under different annealing T (Figure 1f). Two characteristic Raman modes at  $\approx 208$  and  $410\text{ cm}^{-1}$  can be well assigned to the longitudinal optical (LO) and 2 LO phonon modes of 4 ML CdSe NPLs, which is consistent with literature reports.<sup>[41]</sup> By annealing the NPL film at 350 °C, we observe three newly emerged peaks at 290, 392, and  $938\text{ cm}^{-1}$  (marked in green) which can be attributed to CdO.<sup>[42]</sup> Together with the absorption data, we can conclude that along with the formation of bulk CdSe, oxide formation takes place simultaneously by annealing at 350 °C. Formation of CdO likely takes place at the surface of the CdSe aggregates following (partial if not complete) ligand removal.

## 2.4. TEM Analysis

We performed TEM on NPLs films to obtain direct information on the morphology change (e.g., the inter-NPL distance change) after the thermal treatment. The as-prepared 4 ML CdSe NPLs films assemble in an edge-up geometry with a  $3.8 \pm 0.5$  nm face-to-face stacking distance, as shown in Figure 2a,b. This inter-NPL distance is slightly higher than twice the Cd-myristate ligand length (nominally  $\approx 1.7$  nm).<sup>[43]</sup> By further increasing the annealing T, as shown in Figure 2c (for 250 °C) and Figure 2e (for 300 °C), the edge-up configuration is maintained. The inter-NPL distance gradually drops with increasing T. More precisely, we observe that the first decrease in inter-NPL distance occurs at already at a low T, at  $\approx 80$  °C (from 3.8 to  $\approx 2.5$  nm), which is slightly above the evaporation point of the solvent used to disperse the NPLs (hexane, 69 °C). This effect may be related to the evaporation of solvent molecules trapped in the voids of the NPL film, in line with previous reports.<sup>[37]</sup> By further increasing T, the distance remains nearly unchanged until 250 °C, after which it decreases further to below 1 nm at 340 °C. Although irregularly shaped objects were observed at 300 and 340 °C (Figure 2g,i), further XRD studies confirm that the main crystal phase remains zinc blende CdSe NPLs (Figure S5a,b, Supporting Information). These irregularly shaped substances may be assigned to aggregates of decomposed ligands. Finally, the film annealing at 350 °C results in the formation of clusters or the “necking” of NPLs leading to a fused solid (Figure S2, Supporting Information). In this narrow T range, combining the absorption result (i.e., the sudden changes from weak “excitonic” to bulk-like absorption), Raman data (i.e., the emergence of oxidation signal), and TEM analysis, we conclude that ligands are gradually removed from the NPL surface between 250 and 340 °C, and undergo a remarkably sudden removal of residual ligands between 340 and 350 °C.

## 2.5. Thermogravimetric Analysis with Mass-Spectrometry (TGA-MS) Analysis

To better understand the desorption of the potent myristic acid-related capping ligands, we conducted TGA-MS to study the decomposition of Cd(myristate)<sub>2</sub>. In an ideal situation, we would have conducted the study for Cd(myristate)<sub>2</sub> capped 4 ML CdSe NPLs, but we have insufficient CdSe NPLs to do so. Such a simplified study can still provide molecular insights into the effects of thermal treatment. This is because although technical grade oleic acid was applied in the NPL synthesis, a high content of myristic acid is expected to cover the NPLs' surface. Therefore, we believe that the simplified thermogravimetric experiments of myristic acid ligands (without NPLs) should be justified to study the surface ligand decomposition at NPL surfaces. Figure 3a presents the normalized T-dependent gas release kinetics. First, the TGA curve shows two important weight loss steps, with the first step at a temperature range of  $\approx 250$ –350 °C with 62 wt. % loss (the T range that is relevant to our studies). In this region, the recorded gases detected by MS include various oxygen-containing molecules of organic molecules (i.e., CO, CO<sub>2</sub>, and H<sub>2</sub>O), and carbon-rich fragments (such as CH<sub>3</sub>, CH<sub>2</sub>, C<sub>2</sub>H<sub>3</sub>, and C<sub>2</sub>H<sub>2</sub>). Increasing the temperature from 355 to 475 °C results in a second weight loss step with 11% more weight loss (Table S1, Supporting Information).

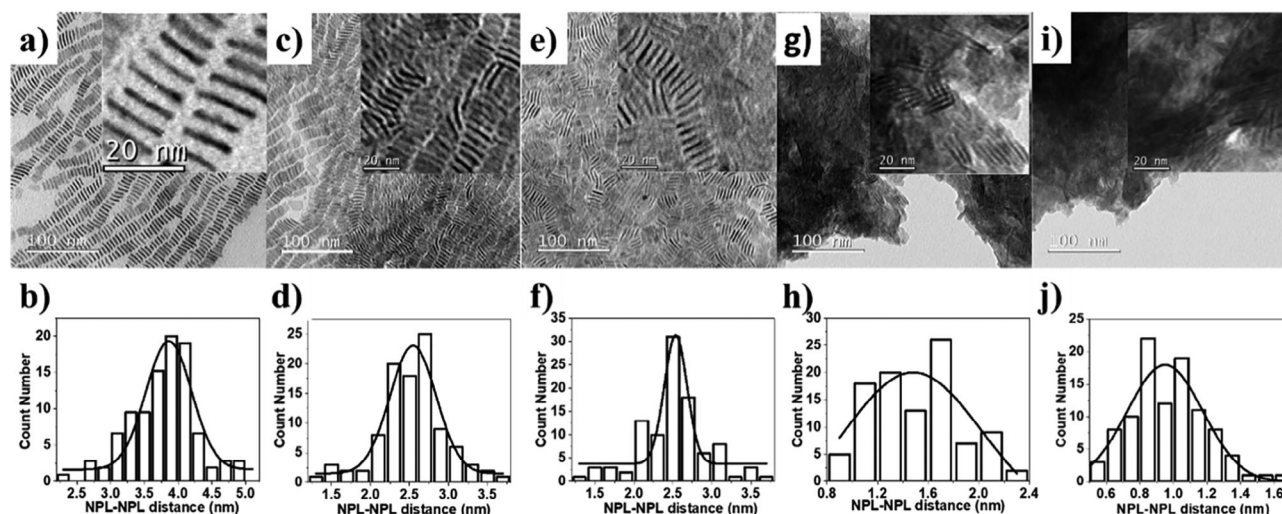


**Figure 2.** TEM images of four ML CdSe NPLs as-synthesized a), after annealing at 80 °C c), 250 °C e), 300 °C g), and 340 °C i). The NPL–NPL distances are  $3.8 \pm 0.5$  nm a),  $2.5 \pm 0.4$  nm c),  $2.5 \pm 0.5$  nm e),  $1.5 \pm 0.4$  nm g), and  $1.0 \pm 0.2$  nm i), respectively. Histograms of the NPL–NPL distance of four ML NPLs as-synthesized b), after annealing at 80 °C d), 250 °C f), 300 °C h), and 340 °C j). Approx 100 NPL–NPL distances were analyzed.

The released gases in the second step are only C and CO<sub>2</sub>. We believe the first decomposition reactions happen during the first step, as most ligands were lost from the NPL solid and turned to gases. Furthermore, based on the MS signals, all the C–H containing parts of the ligands were released in the first step as well, while only C and C–O species were detected in the second step. Finally, given the varied gases (for both oxidized and C-based ones) releases and their similar kinetics, we exclude a scenario in which all the ligands decompose simultaneously in a step-by-step fashion, by losing –CH<sub>3</sub>, or –CH<sub>2</sub>– groups (by simple decomposition or oxidation) one by one.

When we thermally anneal the ligand-capped NPL film in the air, we propose that O<sub>2</sub> oxidizes the Cd-myristate ligands to liberate gases. As a result, the ligand density decreases at high temperatures, thus gradually decreasing the inter-NPL distance. This proposal is consistent with previous reports. David et al. reported the decomposition and fragmentation products of CdSe QDs with the tert-butylthiol ligand.<sup>[33]</sup> Isobutene and isobutane were observed as the major volatile products during TGA measurements, and C<sub>x</sub>H<sub>y</sub> was removed first. This provides a fine control on inter-NPL distance. In addition, SEM-EDX analysis shows

a similar Cd/Se ratio for annealed NPLs, and a reduced amount of C content with increased annealing T, further supporting the conclusion of selectively removing ligands during the thermal annealing process (Table 1). In Figure 3b, we demonstrate that the weight loss by heat treatment can correlate perfectly with the NPL–NPL distance (by TEM) and shifts in the absorption, providing a direct correlation between the thermal decomposition of ligands to the morphology modulation, and as a result, to the physical properties of NPL solids.

## 2.6. Photoconductivity Measurements by THz Spectroscopy

To investigate the effect of the shortened ligand length on the optoelectronic properties following thermal annealing at varied T, we employ contact-free, optical pump-THz probe (OPTP) spectroscopy to measure the time- and frequency-resolved photoconductivity with sub-ps time resolution. The pump-induced change in the conductivity, that is, photoconductivity  $\Delta\sigma$ , is proportional to the photoinduced THz absorption ( $\Delta E = E_{\text{pump}} - E$ ) at varying pump-probe delays, where  $E_{\text{pump}}$  and  $E$  represent the transmitted THz field with and without photoexcitation (See

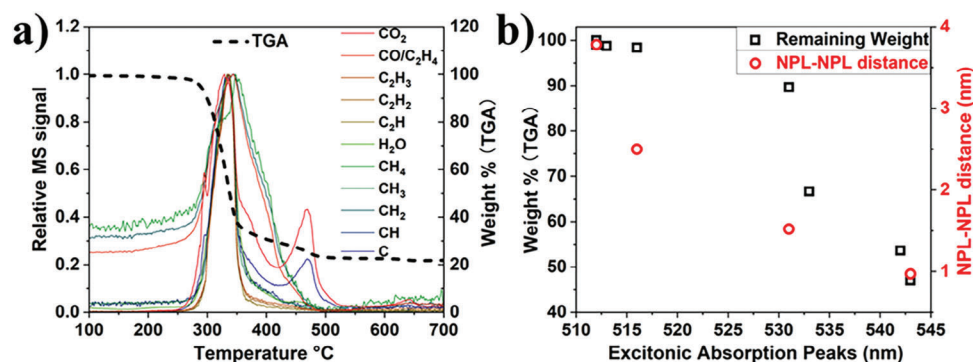


**Figure 3.** a) Thermogravimetric Analysis with Mass-Spectrometry curve for the decomposition of Cd(myristate)<sub>2</sub>. b) Correlation between the TGA weight loss and the NPL–NPL distance versus the excitonic absorption peak for treatments until 340 °C.

**Table 1.** Elemental compositions of as-prepared CdSe NPLs, NPLs-Air-250 °C, and NPLs-Air-300 °C determined by SEM-EDX analysis.

4 ML CdSe NPLs	Cd	Se	C	Cd:Se
Native Myristate Ligand	13.51 wt. %	10.81 wt. %	75.67 wt. %	1.25
250 °C in the air	22.63 wt. %	18.44 wt. %	58.93 wt. %	1.23
300 °C in the air	36.71 wt. %	29.63 wt. %	33.66 wt. %	1.24

Experimental Section). **Figure 4a** compares the photoconductivity dynamics of NPL films annealed at different T, normalized to the absorbed photon densities ( $N_{abs}$ ). Though displaying a similar dynamic evolution within 10 ps, the different films show distinctly varied intensities. Specifically, in line with all the structure and thermal analysis above, with increasing T over 250 °C, the OPTP intensity increases substantially, which is further demonstrated clearly in Figure 4b. Since  $(\Delta\sigma)/N_{abs}$  is proportional to the product of the photon-to-free-carrier quantum yield  $\phi$  and charge mobility  $\mu$ , the enhanced OPTP signal at elevated annealing T is attributed to a higher free carrier population and/or improved charge transport properties. As the averaged ligand length becomes shorter with annealing, the electronic coupling between the adjacent layers increases, which could give rise to an enhanced out-of-plane dielectric screening and reduced quantum confinement. These effects will greatly reduce the exciton binding energy and, thus, raise the proportion of the free electrons and holes. Besides, the out-of-plane charge transport across the adjacent NPLs will increase because of the enhanced inter-NPL electronic coupling. The increase in the carrier mobility observed

at high temperatures is indeed a promising development for electronic devices, such as LEDs, where efficient charge transport is critical. However, it appears that for LED applications, additional measures may be required to passivate defects formed during annealing (Figure S7, Supporting Information), to recover the emission properties.

To confirm and disentangle these two contributions from the free carrier density and charge mobility, we conducted THz time-domain spectroscopic (THz-TDS) analysis at a given pump-probe delay time. THz-TDS provides the frequency-resolved complex photoconductivity spectra, including the real and imaginary parts, as shown in Figure 4c–e. At RT, the photoconductivity spectrum shows an exciton-dominated response with a finite real part and a pronounced negative imaginary part, which can be described by a Lorentz model.<sup>[44]</sup> This is in line with the large exciton binding energy of 170 meV in 4 ML CdSe NPLs with native ligands, which leads to a dominant exciton population. At high annealing T, the photoconductivity spectra change, as illustrated in Figure 4d,e, and are dominated by the real component, indicating the free-carrier-dominated dynamics. The conductivity dispersion can be adequately described by the so-called Drude-Smith model:<sup>[46]</sup>

$$\sigma_{\text{Drude-Smith}} = \frac{\omega_p^2 \epsilon_0 \tau}{1 - i\omega\tau} \left( 1 + \frac{c}{1 - i\omega\tau} \right) \quad (1)$$

Here,  $\tau$ ,  $\omega_p$ , and  $\epsilon_0$  are the effective scattering time, plasma frequency, and vacuum permittivity, respectively. In this model, free carriers dominate the photo-response and experience

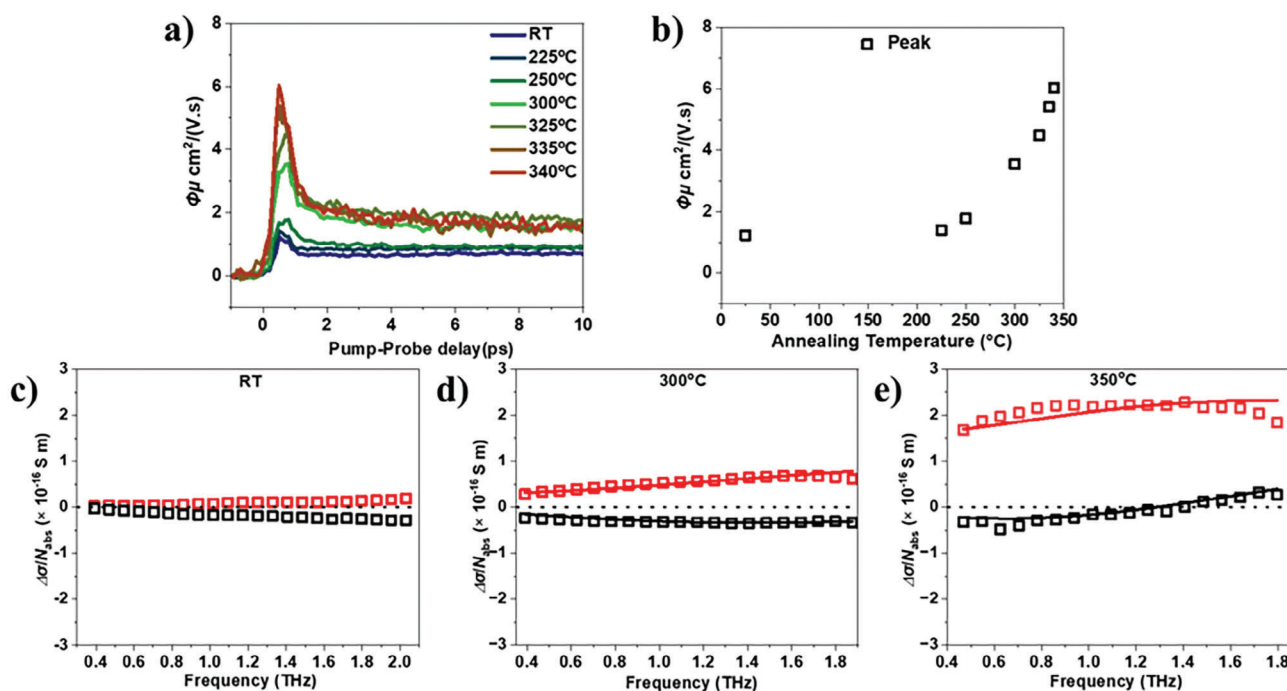


**Figure 4.** a) Annealing-T-dependent photoconductivity dynamics by optical-pump-THz probe (OPTP) spectroscopy following 3.10 eV photoexcitation. b) Normalized OPTP peak in (a) as a function of annealing T. Frequency-resolved photoconductivity spectra of c) 4 ML CdSe NPLs with native ligand, d) NPLs-300 °C and e) NPLs-350 °C, respectively. The data are measured at 0.2 ps after the OPTP peak. The data are fitted by the Drude-Smith model, as described in the main text. The red and black solid lines represent the real and imaginary parts of the complex THz photoconductivity as modeled with the Drude-Smith model, respectively.

**Table 2.** The obtained Drude-Smith parameters for different temperatures.

Annealing temperature [°C]	$\tau$ [fs]	$c$	Carrier density [ $m^{-3}$ ]
250	$43 \pm 3$	$-0.95 \pm 0.01$	$4.17 \times 10^{21} \pm 1 \times 10^{19}$
300	$44 \pm 2$	$-0.87 \pm 0.01$	$8.35 \times 10^{21} \pm 2 \times 10^{19}$
325	$47 \pm 5$	$-0.89 \pm 0.03$	$8.54 \times 10^{21} \pm 5 \times 10^{19}$
335	$49 \pm 4$	$-0.83 \pm 0.01$	$9.08 \times 10^{21} \pm 3 \times 10^{19}$
350	$69 \pm 5$	$-0.67 \pm 0.02$	$12.10 \times 10^{21} \pm 2 \times 10^{19}$

preferential back-scattering resulting from spatial confinement due to, for example, grain boundaries or interfaces.<sup>[45,46]</sup> This effect is evaluated quantitatively by the parameter  $c$  ranging from  $-1$  to  $0$ . When  $c = 0$ , the free carriers undergo a Drude-like transport with a momentum-randomizing scattering; for  $c = -1$ , these free carriers are subject to a complete back-scattering with strong confinement. As shown in **Table 2**, the extracted parameter  $c$  from the fits increases with increasing the annealing  $T$ , which indicates reduced confinement of the photogenerated free carriers as the interlayer distance becomes smaller. When  $T = 350$  °C, there is a significant and sudden jump of the parameter  $c$  and scattering time: for the former, it reduces from close to  $-0.95$  to  $-0.67$ , and for the latter, there is a large increase from  $40$ – $50$  to  $\approx 70$  fs. This result is in line with our expectation, in which a structural transition from quasi-2D to 3D with the complete removal of the interlayer ligands. Both parameters have changed in a direction to substantially enhance the short-range charge carrier mobility at the dc limits, following  $\mu = \frac{e\tau}{m^*} (1 + c)$ , by increasing the annealing  $T$  from  $250$  to  $350$  °C. The free carrier density increases gradually by  $T$ , and the free carrier generation quantum increases by a factor of  $3$  by comparing the carrier density generated at  $250$  to that at  $350$  °C based on the fitting result in **Table 2**.

### 3. Conclusion

In summary, we report that thermal annealing represents an effective strategy to tune the optical absorption and electrical properties of NPL assemblies by controlling the inter-NPL distance. The underlying mechanism for such morphology control lies in the stability of the surface ligands: we observe a direct correlation between the  $T$ -dependent ligand decomposition and the NPL-NPL distance shortening (by TEM), the strong red-shift in the absorption band edge (by UV-vis studies), and furthermore, the enhanced electrical transport within the NPL films. Our results illustrate a straightforward manner to control the interfacial electronic coupling strength for developing functional optoelectronics through thermal treatments.

### Supporting Information

Supporting Information is available from the Wiley Online Library or from the author.

### Acknowledgements

The authors thank the financial support from the Max Planck Society. The authors thank Gunnar Glasser for SEM measurements. S.C. acknowledges the fellowship support from the China Scholarship Council

(201804910790). J.J.G. gratefully acknowledges financial support from an Alexander von Humboldt fellowship.

Open access funding enabled and organized by Projekt DEAL.

### Conflict of Interest

The authors declare no conflict of interest.

### Data Availability Statement

The data that support the findings of this study are available from the corresponding author upon reasonable request.

### Keywords

CdSe nanoplatelets, charge transport, coupling strength, thermal annealing, THz spectroscopy

Received: October 6, 2023

Published online:

- [1] D. V. Talapin, J.-S. Lee, M. V. Kovalenko, E. V. Shevchenko, *Chem. Rev.* **2010**, *110*, 389.
- [2] M. Nasilowski, B. Mahler, E. Lhuillier, S. Ithurria, B. Dubertret, *Chem. Rev.* **2016**, *116*, 10934.
- [3] J. Zito, I. Infante, *Acc. Chem. Res.* **2021**, *54*, 1555.
- [4] J.-H. Choi, H. Wang, S. J. Oh, T. Paik, P. Sung, J. Sung, X. Ye, T. Zhao, B. T. Diroll, C. B. Murray, C. R. Kagan, *Science* **2016**, *352*, 205.
- [5] Y.-H. Kim, J. Park, S. Kim, J. S. Kim, H. Xu, S.-H. Jeong, B. Hu, T.-W. Lee, *Nat. Nanotechnol.* **2022**, *17*, 590.
- [6] Y. Wang, S. R. Kavanagh, I. Burgués-Ceballos, A. Walsh, D. O. Scanlon, G. Konstantatos, *Nat Photonics* **2022**, *16*, 235.
- [7] A. Maier, F. Strauß, P. Kohlschreiber, C. Schedel, K. Braun, M. Scheele, *Nano Lett.* **2022**, *22*, 2809.
- [8] Q. A. Akkerman, T. P. T. Nguyen, S. C. Boehme, F. Montanarella, D. N. Dirin, P. Wechsler, F. Beiglböck, G. Rainò, R. Erni, C. Katan, J. Even, M. V. Kovalenko, *Science* **2022**, *377*, 1406.
- [9] F. Wang, A. Dong, W. E. Buhro, *Chem. Rev.* **2016**, *116*, 10888.
- [10] S. Ithurria, B. Dubertret, *J. Am. Chem. Soc.* **2008**, *130*, 16504.
- [11] A. Riedinger, F. D. Ott, A. Mule, S. Mazzotti, P. N. Knüsel, S. J. P. Kress, F. Prins, S. C. Erwin, D. J. Norris, *Nat. Mater.* **2017**, *16*, 743.
- [12] R. Momper, H. Zhang, S. Chen, H. Halim, E. Johannes, S. Yordanov, D. Braga, B. Blülle, D. Doblas, T. Kraus, M. Bonn, H. I. Wang, A. Riedinger, *Nano Lett.* **2020**, *20*, 4102.
- [13] S. Christodoulou, J. I. Climente, J. Planelles, R. Brescia, M. Prato, B. Martín-García, A. H. Khan, I. Moreels, *Nano Lett.* **2018**, *18*, 6248.
- [14] G. Yang, M. Kazes, D. Oron, *Adv. Funct. Mater.* **2018**, *28*, 1802012.
- [15] S. J. Zelewski, K. C. Nawrot, A. Zak, M. Gladysiewicz, M. Nyk, R. Kudrawiec, *J. Phys. Chem. Lett.* **2019**, *10*, 3459.
- [16] E. V. Shornikova, D. R. Yakovlev, N. A. Gippius, G. Qiang, B. Dubertret, A. H. Khan, A. Di Giacomo, I. Moreels, M. Bayer, *Nano Lett.* **2021**, *21*, 10525.
- [17] P. Geiregat, C. Rodá, I. Tanghe, S. Singh, A. Di Giacomo, D. Lebrun, G. Grimaldi, J. Maes, D. Van Thourhout, I. Moreels, A. J. Houtepen, Z. Hens, *Light: Sci. Appl.* **2021**, *10*, 112.
- [18] A. Yeltik, S. Delikanli, M. Olutas, Y. Kelestemur, B. Guzelturk, H. V. Demir, *J. Phys. Chem. C* **2015**, *119*, 26768.
- [19] P. Bai, A. Hu, Y. Deng, Z. Tang, W. Yu, Y. Hao, S. Yang, Y. Zhu, L. Xiao, Y. Jin, Y. Gao, *J. Phys. Chem. Lett.* **2022**, *13*, 9051.

- [20] Y. Liu, M. Gibbs, J. Puthussery, S. Gaik, R. Ihly, H. W. Hillhouse, M. Law, *Nano Lett.* **2010**, *10*, 1960.
- [21] Y. Gao, M. Aerts, C. S. S. Sandeep, E. Talgorn, T. J. Savenije, S. Kinge, L. D. A. Siebbeles, A. J. Houtepen, *ACS Nano* **2012**, *6*, 9606.
- [22] H. Zhang, J. Jang, W. Liu, D. V. Talapin, *ACS Nano* **2014**, *8*, 7359.
- [23] C. S. S. Sandeep, J. M. Azpiroz, W. H. Evers, S. C. Boehme, I. Moreels, S. Kinge, L. D. A. Siebbeles, I. Infante, A. J. Houtepen, *ACS Nano* **2014**, *8*, 11499.
- [24] C. Giansante, I. Infante, E. Fabiano, R. Grisorio, G. P. Suranna, G. Gigli, *J. Am. Chem. Soc.* **2015**, *137*, 1875.
- [25] W. S. Lee, Y.-G. Kang, M. Sharma, Y. M. Lee, S. Jeon, A. Sharma, H. V. Demir, M. J. Han, W.-K. Koh, S. J. Oh, *Adv. Electron. Mater.* **2022**, *8*, 2100739.
- [26] R. T. Graf, A. Schlosser, D. Zámbo, J. Schlenkrich, P. Rusch, A. Chatterjee, H. Pfnür, N. C. Bigall, *Adv. Funct. Mater.* **2022**, *32*, 2112621.
- [27] T. Galle, D. Spittel, N. Weiß, V. Shamraienko, H. Decker, M. Georgi, R. Hübner, N. Metzko, C. Steinbach, D. Schwarz, V. Lesnyak, A. Eyhmüller, *J. Phys. Chem. Lett.* **2021**, *12*, 5214.
- [28] M. V. Kovalenko, M. Scheele, D. V. Talapin, *Science* **2009**, *324*, 1417.
- [29] J.-S. Lee, M. V. Kovalenko, J. Huang, D. S. Chung, D. V. Talapin, *Nat. Nanotechnol.* **2011**, *6*, 348.
- [30] S. Zhang, P. W. Cyr, S. A. McDonald, G. Konstantatos, E. H. Sargent, *Appl. Phys. Lett.* **2005**, *87*, 233101.
- [31] R. J. Sutton, G. E. Eperon, L. Miranda, E. S. Parrott, B. A. Kamino, J. B. Patel, M. T. Hörantner, M. B. Johnston, A. A. Haghighirad, D. T. Moore, H. J. Snaith, *Adv. Energy Mater.* **2016**, *6*, 1502458.
- [32] F. Palazon, F. Di Stasio, S. Lauciello, R. Krahne, M. Prato, L. Manna, *J. Mater. Chem. C* **2016**, *4*, 9179.
- [33] D. H. Webber, R. L. Brutchey, *J. Am. Chem. Soc.* **2012**, *134*, 1085.
- [34] S. Ithurria, M. D. Tessier, B. Mahler, R. P. S. M. Lobo, B. Dubertret, A. L. Efros, *Nat. Mater.* **2011**, *10*, 936.
- [35] D. Li, C. Wang, D. Tripkovic, S. Sun, N. M. Markovic, V. R. Stamenkovic, *ACS Catal* **2012**, *2*, 1358.
- [36] M. Cargnello, C. Chen, B. T. Diroll, V. V. T. Doan-Nguyen, R. J. Gorte, C. B. Murray, *J. Am. Chem. Soc.* **2015**, *137*, 6906.
- [37] F. Iacono, L. De La Cueva, J. M. Gallego, B. H. Juarez, R. Otero, *Part. Part. Syst. Character.* **2016**, *33*, 358.
- [38] E. Moya, H. Jun, H.-M. Kim, J. Jang, *ACS Appl. Mater. Interfaces* **2018**, *10*, 42647.
- [39] T. Trindade, P. O'Brien, X.-M. Zhang, *Chem. Mater.* **1997**, *9*, 523.
- [40] W. Wu, F. He, Y. Wang, *J. Appl. Phys.* **2016**, *119*, 055701.
- [41] S. A. Cherevko, A. V. Fedorov, M. V. Artemyev, A. V. Prudnikau, A. V. Baranov, *Phys. Rev. B* **2013**, *88*, 041303.
- [42] S. Kumar, A. K. Ojha, *AIP Adv.* **2013**, *3*, 052109.
- [43] C. Tanford, *J. Phys. Chem.* **1972**, *76*, 3020.
- [44] A. Tries, S. Osella, P. Zhang, F. Xu, C. Ramanan, M. Kläui, Y. Mai, D. Beljonne, H. I. Wang, *Nano Lett.* **2020**, *20*, 2993.
- [45] W. Zheng, N. F. Zorn, M. Bonn, J. Zaumseil, H. I. Wang, *ACS Nano* **2022**, *16*, 9401.
- [46] X. Wang, J. Ma, W. Zheng, S. Osella, N. Arisnabarreta, J. Droste, G. Serra, O. Ivasenko, A. Lucotti, D. Beljonne, M. Bonn, X. Liu, M. R. Hansen, M. Tommasini, S. De Feyter, J. Liu, H. I. Wang, X. Feng, *J. Am. Chem. Soc.* **2022**, *144*, 228.